Suppression of Nonlinear Panel Flutter with Piezoelectric Actuators Using Finite Element Method

R.C. Zhou,* Zhihong Lai,† David Y. Xue,‡ Jen-Kuang Huang,§ and Chuh Mei¶
Old Dominion University, Norfolk, Virginia 23529-0247

An optimal control design is presented to actively suppress large-amplitude, limit-cycle flutter motions of rectangular isotropic plates at supersonic speeds using piezoelectric actuators. The nonlinear panel flutter equations based on the finite element method are derived for isotropic plates with piezoelectric layers subjected to aerodynamic and thermal loads. A model reduction is performed to the finite element system equations of motion for the control design and the time domain simulation. An optimal controller is developed based on the linearized modal equations, and the norms of the feedback control gain are employed to provide the optimal shape and location of the piezoelectric actuators. Numerical simulations based on the reduced nonlinear panel flutter model show that the critical dynamic pressure can be increased three to four times by the piezoelectric actuation. Within the increased critical dynamic pressure, the limit-cycle motions can be completely suppressed. The results demonstrate that piezoelectric materials are effective in panel flutter suppression.

Nomenclature

$[A], [B], [D]$	= extension, coupling, and bending panel stiffness matrices
a, b	= panel length and width
C	= modal aerodynamic damping matrix
c_a	= air-panel mass ratio over Mach number
d_{31}	= electromechanical coefficient
E	= Young's modulus
e_3	= electrical field
$[G], [g]$	= system and element aerodynamic damping matrices
g_a	= nondimensional aerodynamic damping
h	= thickness
$[K], [k]$	= system and element linear stiffness matrices
$[K1], [k1]$	= first-order nonlinear stiffness matrices
$[K2], [k2]$	= second-order nonlinear stiffness matrices
k	= feedback control gain matrix
$[M], [m]$	= mass matrices
$\{M\}$	= moment vector
M_∞	= Mach number
$\{N\}$	= inplane force vector
$\{P\}, \{p\}$	= load vectors
p_a	= aerodynamic pressure
q	= modal amplitude vector
ΔT	= temperature change
u, v, w	= displacements
α	= thermal expansion coefficient
$\{\epsilon\}$	= strain vector
$\{\kappa\}$	= curvature vector
λ	= nondimensional dynamic pressure
μ	= air-panel mass ratio
ν	= Poisson's ratio
$\{\sigma\}$	= stress vector
τ	= nondimensional time
Φ	= modal matrix

Subscript

cr	= critical

Introduction

PANEL flutter at supersonic speeds has been encountered in the operation of aircraft and missiles. The earliest reported structural failures that can be attributed to panel flutter were the failure of the 60–70 early German V-2 rockets during World War II.[1] A recent panel flutter failure was reported on the F-117A.[2] After flight tests of the F-117A stealth fighter, cracks due to flutter (also sonic fatigue) were found in about half of the laminated composite skin panels. Those panels were then redesigned and stiffened and, thus, a tremendous weight penalty was paid.

Panel flutter has received resurgent interest due to the development of high-speed flight vehicles such as the YF-22 advanced tactical fighter, high-speed civil transport (HSCT), and National Aerospace Plane (NASP). When a flight vehicle travels at high speeds, the onset of flutter may be imminent, but usually the dynamic pressure is not the only form of excitation. The friction from the surrounding air causes increased heating of the panel. The presence of high-temperature load results in a flutter motion at lower critical dynamic pressure (λ_{cr}). In addition, the temperature rise may also cause large aerodynamic-thermal deflections of the skin panels, and, thus, affects flutter response and aircraft performance. Most recently, Gray and Mei[3] gave a complete survey on various theoretical considerations and analytical methods for the investigation of nonlinear panel flutter up to 1991. The limit-cycle results obtained from the finite element[3] and classical continuum methods[4] agreed very well with the experiment data by Dowell.[5] The classical analytical method employs, in general, Galerkin's approach in the spatial domain, and the panel deflection is expressed in terms of the linear normal modes; direct numerical integration is then applied in the time domain. Dowell[4] also determined that four or six linear modes are required for obtaining a converged limit-cycle amplitude and frequency.

During the past few years, a significant amount of research has been reported in the field of control of flexible structures by the use of smart sensors and actuators.[6] Piezoelectric materials can develop an electrical charge when subjected to a mechanical strain. The converse piezoelectric effect, development of mechanical strain when subjected to an electrical field, can be utilized to actuate a structure. Thus, actuation of a structure may be accomplished at the material level. Piezoelectric materials in current use include

poly-vinylidene fluoride (PVDF), a semicrystalline polymer film, and lead zirconate titanate (PZT), a piezoelectric ceramic material. PZT generally is stiffer and has large electromechanical coupling coefficients and is, thus, better suited for actuator applications. The film product (PVDF), on the other hand, has higher voltage limits with lower stiffness and coupling coefficients and is, thus, better for sensor applications. Piezoelectric layers bonded to the surface of, or manufactured and embedded into, flexible structure members can act as either control actuators or sensors. The effectiveness of using passive or active control of smart systems has been demonstrated by many researchers. However, most of the control designs have been applied to the linear beam-like and truss structures.

In the area of control of panel flutter response using smart materials, only a few research papers have been reported.[7,8] In Ref. 7, the linear panel flutter control using piezoelectrics was studied. The bending moment induced by the piezoelectrics is not effective to control the linear panel flutter since there is no bending behavior in the linear case. On the other hand, the induced in-plane force is not sufficient in linear panel flutter control because of the low modulus and limited ability of the piezoelectrics to create large in-plane force. In Ref. 8, the panel flutter has been extended to nonlinear. The induced bending moment, therefore, is effective in the nonlinear panel flutter control. However, the classic continuum approach was adopted in their study, which has certain limitations that the panels are of simple geometry and boundary conditions. In addition, the piezoelectric materials in Refs. 7 and 8 have to cover the surfaces of the panel completely since the classic modeling techniques were employed. In the present work, however, the more versatile finite element method is applied. This method can deal with panels of arbitrary geometry and complex boundary conditions. The actuators can be designed in arbitrary shape.

This paper presents an optimal control method to suppress the panel limit-cycle motions at dynamic pressures $\lambda > \lambda_{cr}$ using piezoelectric actuators. The finite element method and the linear optimal control theory are employed for designing the actuator shape and location. The nonlinear dynamic equations of motion, based on von Kármáns large-deflection theory, are developed for panels with symmetrically placed piezoelectric layers subjected to aerodynamic and thermal loads. A model reduction and modal transformation is then performed to obtain a set of coupled nonlinear equations of motion in the modal coordinates. By using the optimal control theory, control actions can be determined based on the linearized modal equations of motion, and the dynamic system will be stable with small perturbations. Because of the limitation of the maximum operating electric field (set at one-half of depolarization in this study) of the piezoelectric actuator, there exists a maximum dynamic pressure above which the flutter motions can no longer be suppressed. The optimal shape and location of the piezoelectric actuators are determined by using the norms of the feedback control gain (NFCG). One-set and two-set completely ($x_s = a$) or partially covered piezoelectric (symmetrically placed) actuators are considered as shown in Fig. 1. Numerical simulations based on the nonlinear modal equations are performed to demonstrate the effectiveness of panel flutter suppression under
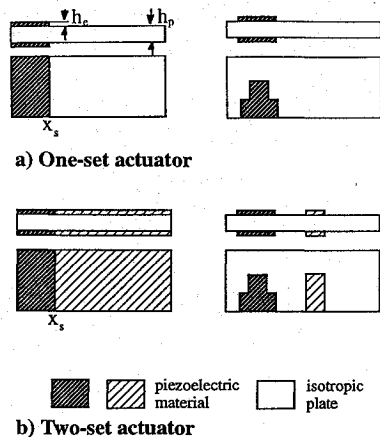
the piezoelectric actuation. The performance of the actuator designs and the maximum flutter-free dynamic pressure are investigated and presented. The contributions of the present work are the investigation of nonlinear panel flutter suppression by an extension of the finite element method and the determination of optimal actuator shape and location using the NFCG criterion.

Finite Element Equations of Motion

As disclosed in panel flutter surveys, the aerodynamic theory employed the most for panel flutter at supersonic flow ($M_\infty > \sqrt{2}$) is the quasisteady, first-order piston theory.[1,3-5] The aerodynamic pressure can be expressed as

$$p_a = -\frac{2q_a}{\beta}\left(\frac{\partial w}{\partial x} + \left(\frac{M_\infty^2 - 2}{M_\infty^2 - 1}\right)\frac{1}{V_\infty}\frac{\partial w}{\partial t}\right)$$

$$= -\left(\lambda\frac{D}{a^3}\frac{\partial w}{\partial x} + \frac{g_a}{\omega_0}\frac{D}{a^4}\frac{\partial w}{\partial t}\right) \tag{1}$$

where $q_a = \rho_a V_\infty^2/2$ is the dynamic pressure, ρ_a is the air mass density, V_∞ is the free stream airflow speed, $\beta = \sqrt{M_\infty^2 - 1}$, and w is the transverse displacement of panel. The nondimensional dynamic pressure is given by

$$\lambda = \frac{2q_a a^3}{\beta D} \tag{2}$$

where D is the bending rigidity of the panel, and $\omega_0 = (D/m_0 a^4)^{\frac{1}{2}}$ is a convenient reference frequency. Another commonly used nondimensional parameter is the air-panel mass ratio[4] which is defined as

$$\mu = \rho_a a/m_0 \tag{3}$$

where m_0 is the average mass density per unit area of panel. For the aerodynamic damping term, two nondimensional coefficients are defined as follows:

$$c_a = \left(\frac{M_\infty^2 - 2}{M_\infty^2 - 1}\right)^2\left(\frac{\mu}{\beta}\right), \qquad g_a = \sqrt{\lambda c_a} \tag{4}$$

and $c_a \approx \mu/M_\infty$ for $M_\infty \gg 1$ as in Ref. 4.

In the derivation of the equations of motion, it is assumed that the panel is thin, i.e., the ratio of length or width over thickness of the panel is greater than 50. In-plane inertia, rotary inertial and transverse shear deformation effects are, thus, negligible. Von Kármán's nonlinear strain-displacement relationships are given by

$$\{\epsilon\} = \left\{\begin{array}{c}\epsilon_x \\ \epsilon_y \\ \gamma_{xy}\end{array}\right\} = \left\{\begin{array}{c}u_{,x} \\ v_{,y} \\ u_{,y}+v_{,x}\end{array}\right\} + \frac{1}{2}\left\{\begin{array}{c}w_{,x}^2 \\ w_{,y}^2 \\ 2w_{,x}\,w_{,y}\end{array}\right\}$$

$$- z\left\{\begin{array}{c}w_{,xx} \\ w_{,yy} \\ 2w_{,xy}\end{array}\right\} = \{\epsilon_m^0\} + \{\epsilon_\theta^0\} + z\{\kappa\} \tag{5}$$

where the membrane strain components $\{\epsilon_m^0\}$ and $\{\epsilon_\theta^0\}$ are due to in-plane displacements and large deflections, respectively.

For an aircraft panel consisting of an isotropic plate with piezoelectric layers on both surfaces of the plate subjected to a uniform temperature change of ΔT, the stress–strain relationships of the isotropic plate are given by

$$\{\sigma\}_p = \left\{\begin{array}{c}\sigma_x \\ \sigma_y \\ \tau_{xy}\end{array}\right\}_p = [E]_p\{\epsilon\} - \left(\frac{E\alpha}{1-\nu}\right)_p\left\{\begin{array}{c}1 \\ 1 \\ 0\end{array}\right\}\Delta T \tag{6}$$

a) One-set actuator

b) Two-set actuator

piezoelectric material   isotropic plate

Fig. 1 Panel configurations.

and the stress–strain relationships of the isotropic piezoelectric layer can be written as

$$\{\sigma\}_e = \begin{Bmatrix} \sigma_x \\ \sigma_y \\ \tau_{xy} \end{Bmatrix}_e = [E]_e\{\epsilon\} - \left(\frac{E\alpha}{1-\nu}\right)_e \begin{Bmatrix} 1 \\ 1 \\ 0 \end{Bmatrix} \Delta T$$

$$- \left(\frac{Ed_{31}}{1-\nu}\right)_e \begin{Bmatrix} 1 \\ 1 \\ 0 \end{Bmatrix} e_3 \tag{7}$$

where the subscripts p and e denote plate and piezoelectric layers, respectively. The last term in Eq. (7) represents the induced stress due to the applied piezoelectric field e_3. The stiffness matrix is given as

$$[E] = \frac{E}{1-\nu^2} \begin{bmatrix} 1 & \nu & 0 \\ \nu & 1 & 0 \\ 0 & 0 & (1-\nu)/2 \end{bmatrix} \tag{8}$$

For a general kth layer, either the isotropic plate ($k = 2$ and $e_3 = d_{31} = 0$) or the piezoelectric layer ($k = 1, 3$), the stress–strain relations can be expressed as

$$\{\sigma\}_k = [E]_k\{\epsilon\} - \left(\frac{E\alpha}{1-\nu}\right)_k \begin{Bmatrix} 1 \\ 1 \\ 0 \end{Bmatrix} \Delta T - \left(\frac{Ed_{31}}{1-\nu}\right)_k \begin{Bmatrix} 1 \\ 1 \\ 0 \end{Bmatrix} e_{3k} \tag{9}$$

The in-plane force and moment resultants, per unit length, are defined as

$$(\{N\}, \{M\}) = \int_{-h/2}^{h/2} \{\sigma\}_k (1, z)\, dz \tag{10}$$

which lead to the constitutive relations for a panel consisting of isotropic and piezoelectric layers as

$$\begin{Bmatrix} N \\ M \end{Bmatrix} = \begin{bmatrix} A & B \\ B & D \end{bmatrix} \begin{Bmatrix} \epsilon^0 \\ \kappa \end{Bmatrix} - \begin{Bmatrix} N_{\Delta T} \\ M_{\Delta T} \end{Bmatrix} - \begin{Bmatrix} N_e \\ M_e \end{Bmatrix} \tag{11}$$

where $\{\epsilon^0\}(= \{\epsilon_m^0\} + \{\epsilon_\theta^0\})$ is the membrane strain, and the panel stiffness matrices are given by

$$([A], [B], [D]) = \int_{-h/2}^{h/2} [E]_k (1, z, z^2)\, dz \tag{12}$$

The thermal and the piezoelectric force and moment vectors, per unit length, are

$$(\{N_{\Delta T}\}, \{M_{\Delta T}\}) = \int_{-h/2}^{h/2} \left(\frac{E\alpha}{1-\nu}\right)_k \begin{Bmatrix} 1 \\ 1 \\ 0 \end{Bmatrix} \Delta T (1, z)\, dz \tag{13}$$

$$(\{N_e\}, \{M_e\}) = \int_{-h/2}^{h/2} \left(\frac{Ed_{31}}{1-\nu}\right)_k \begin{Bmatrix} 1 \\ 1 \\ 0 \end{Bmatrix} e_{3k} (1, z)\, dz \tag{14}$$

The element matrices and equations of motion are derived using the principle of virtual work

$$\delta W = \delta W_{\text{int}} - \delta W_{\text{ext}} = 0 \tag{15}$$

The internal virtual work, considered first, is in general

$$\delta W_{\text{int}} = \int_A [\{\delta\epsilon^0\}^T \{N\} + \{\delta\kappa\}^T \{M\}]\, dA \tag{16}$$

where A is the element area. The virtual work of the external forces, due to the inertia force and the aerodynamic pressure, is given by

$$\delta W_{\text{ext}} = \int_A \left[\delta w \left(p_a - m_0 \frac{\partial^2 w}{\partial t^2}\right)\right] dA \tag{17}$$

The plate bending element employed in the present study is the C^1 conforming rectangular element with total of 24 nodal degrees of freedom (DOF). The 16 element bending displacements at the four nodes are

$$\{w_b\}^T = \{w_1, w_2, w_3, w_4, w_{x1}, w_{x2}, w_{x3}, w_{x4},$$

$$w_{y1}, w_{y2}, w_{y3}, w_{y4}, w_{xy1}, w_{xy2}, w_{xy3}, w_{xy4}\} \tag{18}$$

The eight element membrane nodal displacements are

$$\{w_m\}^T = \{u_1, u_2, u_3, u_4, v_1, v_2, v_3, v_4\} \tag{19}$$

and the element membrane displacement functions, u and v, are both linear function in x and y.

With the application of virtual work, Eqs. (15–17), and the use of finite element expressions, the element equations of motion subjected to a dynamic pressure, temperature change, and electrical field can be expressed as

$$\frac{1}{\omega_0^2} \begin{bmatrix} [m_b] & 0 \\ 0 & 0 \end{bmatrix} \begin{Bmatrix} \ddot{w}_b \\ \ddot{w}_m \end{Bmatrix} + \frac{g_a}{\omega_0} \begin{bmatrix} [g] & 0 \\ 0 & 0 \end{bmatrix} \begin{Bmatrix} \dot{w}_b \\ \dot{w}_m \end{Bmatrix}$$

$$+ \left(\lambda \begin{bmatrix} [a_a] & 0 \\ 0 & 0 \end{bmatrix} + \begin{bmatrix} [k_b] & [k_B]_{bm} \\ [k_B]_{mb} & [k_m] \end{bmatrix} - \begin{bmatrix} [k_{N\Delta T}] & 0 \\ 0 & 0 \end{bmatrix}\right.$$

$$- \begin{bmatrix} [k_{Ne}] & 0 \\ 0 & 0 \end{bmatrix} + \begin{bmatrix} [k1_{Nm}]_b + [k1_{NB}]_b & [k1]_{bm} \\ [k1]_{mb} & 0 \end{bmatrix}$$

$$+ \begin{bmatrix} [k2] & 0 \\ 0 & 0 \end{bmatrix}\right) \begin{Bmatrix} w_b \\ w_m \end{Bmatrix} = \begin{Bmatrix} p_{b\Delta T} \\ p_{m\Delta T} \end{Bmatrix} + \begin{Bmatrix} p_{be} \\ p_{me} \end{Bmatrix} + \{f\} \tag{20}$$

where $\{f\}$ is the internal equilibrium force vector. The subscripts b and m denote bending and membrane components, respectively; the subscripts B, $N\Delta T$, Ne, Nm, NB, ΔT, and e denote that the corresponding stiffness matrix or load vector is due to the extension-bending coupling stiffness matrix $[B]$, thermal membrane force $\{N_{\Delta T}\}$, piezoelectric membrane force $\{N_e\}$, membrane forces $\{N_m\}(= [A]\{\epsilon_m^0\})$ and $\{N_B\}(= [B]\{\kappa\})$, and thermal ΔT and piezoelectric field e_3, respectively. All of the element matrices in Eq. (20) are symmetrical except the aerodynamic influence matrix $[a_a]$ which is skewsymmetric. The detailed derivation of element mass, thermal and piezoelectric geometric stiffness ($[k_{Ne}]$ and $[k_{N\Delta T}]$ are similar), nonlinear stiffness matrices, and load vectors ($\{p_{be}\}$ and $\{p_{b\Delta T}\}$ or $\{p_{me}\}$ and $\{p_{m\Delta T}\}$ are similar) are given in Refs. 9–11.

By summing up the contributions from all of the elements and taking account of the panel kinematic boundary conditions, the system equations of motion for a given rectangular panel can be written as

$$\frac{1}{\omega_0^2} \begin{bmatrix} [M_b] & 0 \\ 0 & 0 \end{bmatrix} \begin{Bmatrix} \ddot{W}_b \\ \ddot{W}_m \end{Bmatrix} + \frac{g_a}{\omega_0} \begin{bmatrix} [G] & 0 \\ 0 & 0 \end{bmatrix} \begin{Bmatrix} \dot{W}_b \\ \dot{W}_m \end{Bmatrix}$$

$$+ \left(\lambda \begin{bmatrix} [A_a] & 0 \\ 0 & 0 \end{bmatrix} + \begin{bmatrix} [K_b] & [K_B]_{bm} \\ [K_B]_{mb} & [K_m] \end{bmatrix} - \begin{bmatrix} [K_{N\Delta T}] & 0 \\ 0 & 0 \end{bmatrix}\right.$$

$$- \begin{bmatrix} [K_{Ne}] & 0 \\ 0 & 0 \end{bmatrix} + \begin{bmatrix} [K1_{Nm}]_b + [K1_{NB}]_b & [K1]_{bm} \\ [K1]_{mb} & 0 \end{bmatrix}$$

$$+ \begin{bmatrix} [K2] & 0 \\ 0 & 0 \end{bmatrix}\right) \begin{Bmatrix} W_b \\ W_m \end{Bmatrix} = \begin{Bmatrix} P_{b\Delta T} \\ P_{m\Delta T} \end{Bmatrix} + \begin{Bmatrix} P_{be} \\ P_{me} \end{Bmatrix} \tag{21}$$

Equation (21) can be simplified considerably if we design the panel with certain rules. Figure 1 shows panels containing one-set and two-set piezoelectric layers of equal thickness placed symmetrically with respect to the midplane of the plate. For the present symmetrical panel configurations under a steady-state uniform temperature distribution ΔT, the stiffness matrices due to the coupling stiffness $[B]$ and the thermal bending load vector are all null, that is, $[K_B]_{bm} = [K_B]_{mb} = [K1_{NB}]_b = \{P_{b\Delta T}\} = 0$. Then Eq. (21) can be simplified by substituting the membrane displacements in terms of

the bending displacements. The dynamic equations of motion can be expressed by collecting the terms as

$$\left(1/\omega_0^2\right)[M_b]\{\ddot{W}_b\} + (g_a/\omega_0)[G]\{\dot{W}_b\} + ([\bar{K}] + [\overline{K1}]$$

$$+ [\overline{K2}])\{W_b\} = \{P_{be}\} \tag{22}$$

where $[M_b]$ and $[G]$ are the panel mass and aerodynamic damping matrices, respectively, and $\{P_{be}\}$ is the piezoelectric load vector. The detailed expressions of the matrices $[\bar{K}]$, $[\overline{K1}]$ and $[\overline{K2}]$ are given in Appendix A.

Model Reduction and Modal Equations

The system equation of motion presented in Eq. (22) is not suitable for control design; 1) the order the DOF of the system displacement vector $\{W_b\}$ is usually too large, and 2) the nonlinear stiffness matrices, $[\overline{K1}]$ and $[\overline{K2}]$ are functions of the system displacement vector. Therefore, Eq. (22) has to be transformed into a set of properly chosen modal coordinates with much smaller and manageable degrees of freedom (say, less than 10). This is accomplished by a modal transformation

$$\{W_b\} = \sum_{r=1}^{n}\sum_{s=1}^{m} q_{rs}(t)\{\phi_{rs}\} \tag{23}$$

where q_{rs} is the modal amplitude, and $\{\phi_{rs}\}$ is the corresponding (r, s) normal mode which can be obtained from the panel linear vibration

$$(\omega_{rs}/\omega_0)^2[M_b]\{\phi_{rs}\} = [K_b]\{\phi_{rs}\} \tag{24}$$

For a rectangular panel with airflow along its length, the proper mode in the spanwise direction is only the first mode ($m = 1$), (Refs. 4 and 7), and Eq. (23) becomes

$$\{W_b\} = \sum_{r=1}^{n} q_r(t)\{\phi_r\} = \Phi q \tag{25}$$

The system equations of motion, Eq. (22), are transferred into the forced Duffing equations in reduced modal coordinates, thus, they become

$$M\frac{d^2q}{d\tau^2} + C\frac{dq}{d\tau} + (K + K_e + K_{qq})q = F \tag{26}$$

where $\tau = \omega_0 t$ is the nondimensional time, the modal mass M and aerodynamic damping C matrices both are diagonal, K and K_e are the linear modal stiffness matrices, K_{qq} is quadratic in terms of the modal coordinates q, and F is the modal force vector. The transformation of the system equations from the bending displacements, Eq. (22), to the modal coordinates q, Eq. (26), is given in Appendix B. The piezoelectric geometric modal stiffness matrix K_e, Eq. (B10), is due to the piezoelectric inplane force only, whereas the modal force vector F, Eq. (B12), is related to the induced piezoelectric bending moment.

The piezoelectric actuator configurations of the present design in Fig. 1 consist of one- and two-set actuations. Each actuator set (top and bottom layers) can be stimulated such that when one layer contracts, another expands, to create bending moment and in-plane force if the stresses induced by electric fields in the top and bottom layers are not balanced. For the one-set actuator, for example, the electric field e_{3t} applied to the top layer of the actuator set can be expressed as

$$e_{3t} = e_m + e_b \tag{27}$$

and the electric field e_{3b} applied to the bottom layer of actuator set can be expressed as

$$e_{3b} = e_m - e_b \tag{28}$$

where e_m and e_b represent electric fields for in-plane force and bending moment, respectively. If we assume that the top and bottom piezoelectric layers have the same thickness and material properties, then the matrix K_e is a function of the electric field e_m only,

or its normalized form $U_m = e_m/e_{3\max}$; F is only a function of the electric field e_b, or its normalized form $U_b = e_b/e_{3\max}$, where $e_{3\max}$ is the maximum operating (set at one-half of depolarization) electric field of the piezoelectric material. For N-set piezoelectric actuators, therefore, the reduced modal equations of motion can be expressed as

$$M\frac{d^2q}{d\tau^2} + C\frac{dq}{d\tau} + (K + K_e + K_{qq})q = GU_b \tag{29}$$

where G is the control influence matrix which is related to the piezoelectric actuators and can be found in Appendix C.

Optimal Control Design

For suppression of panel flutter limit-cycle motions, an optimal control approach based on the linear optimal control theory is proposed. The linear panel flutter is unstable when $\lambda > \lambda_{cr}$, whereas the nonlinear panel flutter is a stable limit-cycle oscillation. Since the flutter is caused by this instability of the linear model, the goal of control design is to keep the system stable. Thus, the stable nonlinear system would be controllable. The linear model is obtained by ignoring the nonlinear term from Eq. (29):

$$M\frac{d^2q}{d\tau^2} + C\frac{dq}{d\tau} + (K + K_e)q = GU_b \tag{30}$$

For control design using both in-plane forces and bending moments, the stiffness matrix K_e varies with U_m, and makes the problem complicated. The problem can be simplified by first using a constant U_m. Then the control variable becomes U_b, which induces bending moment only. The equations of motion can be written as

$$\frac{dX}{d\tau} = AX + BU \tag{31}$$

where

$$X = \begin{bmatrix} q \\ \dfrac{dq}{d\tau} \end{bmatrix}, \qquad A = \begin{bmatrix} 0 & I \\ -M^{-1}(K + K_e) & -M^{-1}C \end{bmatrix}$$

$$B = \begin{bmatrix} 0 \\ M^{-1}G \end{bmatrix}, \qquad U = U_b$$

The linear quadratic performance index for optimal control can be formulated as

$$J = \frac{1}{2}\int_0^\infty (X^T QX + U^T RU)\,d\tau \tag{32}$$

where Q is a positive semidefinite state penalty matrix, and R is a positive definite control penalty matrix. From the optimal control theory, the optimal controller for this linear quadratic regulator problem is

$$U = -R^{-1}B^T PX \tag{33}$$

where P is a positive definite matrix obtained from the following Riccati equation[12]:

$$A^T P + PA - PBR^{-1}B^T P = -Q \tag{34}$$

There are many ways to select for the weighting matrix Q as long as it is positive semidefinite. The energy weighting is one of the common selections. Thus, the matrix Q consists of the kinetic and potential energy of the system as

$$Q = \begin{bmatrix} K & 0 \\ 0 & M \end{bmatrix} \tag{35}$$

Because of the limitation of the maximum electric field that can be applied to the piezoelectric material, for a given U_{mi}, there is a constraint for the normalized control variable

$$|U_{bi}| \le 1 - |U_{mi}|, \quad i = 1, 2, \dots, N \tag{36}$$

where N is the number of piezoelectric actuator sets. For different constant U_m, an optimal feedback control gain for U_b can be obtained. Finally, an optimal set of U_m and U_b can be determined.

From Eq. (33), the feedback control gain is defined as

$$k = -R^{-1}B^T P \qquad (37)$$

The norms of the feedback control gain are used to determine the location and shape of the piezoelectric actuators. The NFCG can be defined as

$$\text{NFCG} = \sqrt{\sum_{j=1}^{2n} k_{ij}^2}, \quad i = 1, 2, ..., N \qquad (38)$$

where 2n is the total number of state variables defined in Eq. (31).

The piezoelectric layers are first divided into a number of small patches which are equal to the number of the finite elements used. The norm is then calculated for each patch using Eq. (38). The higher the value of norm is, the more control influence that particular element has. The piezoelectric patch is then placed to that location. By connecting these patches, the shape and location of piezoelectric actuator can be obtained. This will be addressed in detail in the following section.

Numerical Simulations

The numerical simulation is based on a rectangular aluminum plate with symmetrically placed piezoelectric layers (Fig. 1). All four edges of the plate are either simply supported or clamped. The C^1 conforming rectangular plate element is used in the finite element model, and the panel is modeled as 10×3 (30 rectangular elements) mesh for half-plate due to symmetry shown in Fig. 2.

The in-plane displacements at the edges are considered to be completely immovable, i.e., $u(0, y) = u(a, y) = v(x, -b/2) = v(x, b/2) = 0$. The physical parameters and the geometry of the plate are $a = 12$ or 24 in., $b = 12$ in., $h = 0.080$ in., $h_p = 0.050$ in., $h_e = 0.015$ in., and $c_a = 0.01$ or 0.1. The material properties of the aluminum plate and the piezoelectric material are as follows. For the aluminum plate $E_p = 1.0 \times 10^7$ psi, $\nu_p = 0.3$, $\rho_p = 0.2588 \times 10^{-3}$ lb-s^2/in.^{4}, and $\alpha_p = 12.5 \times 10^{-6}$ 1/°F. For the piezoelectric layer $E_e = 0.9 \times 10^7$ psi, $\nu_e = 0.3$, $\rho_e = 0.7101 \times 10^{-3}$ lb-s^2/in.^{4}, $\alpha_e = 3 \times 10^{-6}$ 1/°F, $d_{31} = -7.51 \times 10^{-9}$ in./V, and $e_{3\max} = 1.52 \times 10^4$ V/in.

In-Plane Force

Flutter suppression by induced piezoelectric in-plane force only (no bending moment) with a one-set completely covered piezoelectric actuator is investigated first. Figure 3 shows an increase of the critical dynamic pressure for a simply supported square panel. The normalized electric field, $e_m/e_{3\max}$, varies from 0 to 1. When setting the electric field e_m to its maximum $e_{3\max}$ the in-plane force reaches to its maximum. On the other hand, when setting e_m to zero the in-plane force is also zero. The critical dynamic pressure is increased less than 25% by setting $e_m/e_{3\max}$ to one. This is because the in-plane force induced by piezoelectric actuators is small. Therefore, the in-plane force is not efficient in panel flutter control. In the rest of the simulations, the electric field for in-plane force e_m is set equal to zero. This can be achieved since the voltages applied to the top and bottom piezoelectric layers can be equal in magnitudes and opposite in signs. Thus, only bending moment will be produced.

Time History and $\lambda_{\max}$

An optimal control theory is applied to achieve the panel flutter suppression by using piezoelectric actuators with induced bending moments only. The finite element time domain–modal formulation for panel flutter[11] is first solved to yield a limit-cycle motion by the use of the Runge–Kutta method. The panel deflection is represented by six linear modes ($n = 6$) in Eq. (25). Nonlinear equations of motion, Eq. (26), are used for all of the numerical simulations. Optimal control design is based on linear modal equations of motion and is performed for every dynamic pressure. The weighting matrix R is chosen as an identity matrix times a positive constant.
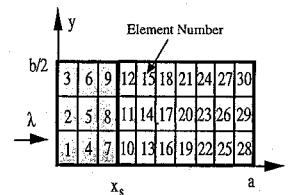

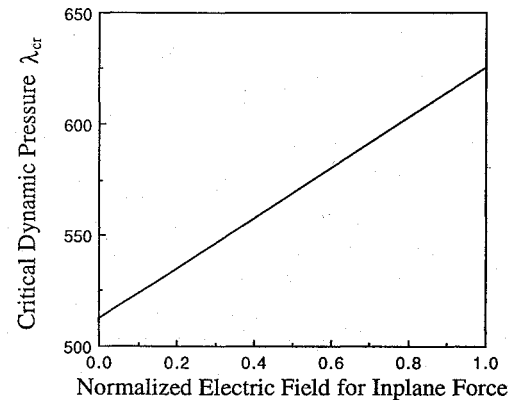Fig. 2   Finite element mesh, half-plate model.

Fig. 3   Critical dynamic pressure vs in-plane force for a simply supported square panel, $c_a = 0.01$.
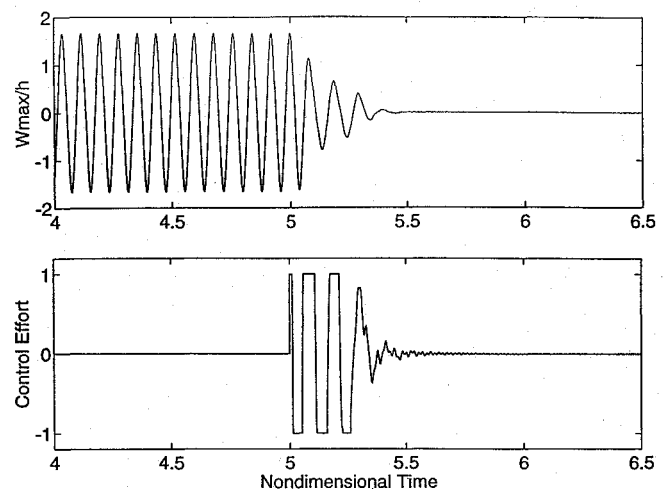

Fig. 4   Time history of limit-cycle amplitude and control effort with one-set completely covered actuator for a simply supported square panel at $\lambda = 1420, c_a = 0.01$.

Figure 4 shows the time history of the plate deflection with the one-set completely covered actuator design. The time response of the plate deflection demonstrates a limit-cycle motion at $\lambda = 1420$ in the beginning. The plate deflection is shown to be suppressed within several cycles after the controller is activated.

The maximum flutter-free dynamic pressure $\lambda_{\max}$ is defined as the maximum λ under which the flutter can be completely suppressed with piezoelectric actuations. The numerical simulations show that the flutter can be suppressed completely below $\lambda_{\max}$ by using the constant control feedback gain properly designed at the $\lambda_{\max}$. The ratio of $\lambda_{\max}$ to λ_{cr} is a good indicator for the performance or effectiveness of the piezoelectric actuator design.

One-Set Actuator

The one-set piezoelectric actuator placed at the leading edge of the plate is studied first. The percentage of piezoelectric material covered (x_s/a) can be varied. The critical dynamic pressure, maximum flutter-free dynamic pressure at $x_s/a = 0.2, 0.5$, and 0.8 are shown in Table 1. The $\lambda_{\max}/\lambda_{cr}$ ratios indicate that more piezoelectric material does not necessarily improve the performance.

Figure 5 gives the values NFCG for a simply supported squared isotropic plate $(a/b = 1)$ by considering the piezo at each element

Table 1 Simply supported square isotropic plate with one-set piezoelectric actuator placed at the leading edge, $c_a = 0.01$

x_s/a	0.2	0.5	0.8
λ_{cr}	165	277	383
λ_{max}	533	1025	1249
$\lambda_{max}/\lambda_{cr}$	3.2	3.7	3.3

Table 2 Simply supported square isotropic plate with one-set partially covered piezoelectric actuator with different NFCG, $c_a = 0.01$

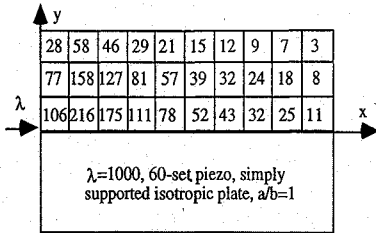| NFCG$\geq$ $\left(\frac{piezo}{total\ area}\right)$	50 (0.40)	60 (0.30)	80 (0.23)	100 (0.20)	120 (0.14)	160 (0.07)
λ_{cr}	265	246	215	203	176	163
λ_{max}	845	745	799	813	713	498
$\lambda_{max}/\lambda_{cr}$	3.2	3.0	3.7	4.0	4.1	3.1

Fig. 5 Norms of feedback control gain for a simply supported square plate, $c_a = 0.01$.

as a single actuator. There are total 30 actuators for 30 elements. The higher the norm is, the more control influence of that corresponding patch is. Based on this criterion, several boundaries for the NFCG have been set up. For example, by considering elements 1, 4, 5, 7, 8, and 10 (see Fig. 2) as one patch for NFCG greater than 100, we can generate a shape for the piezo patch. Using this as a design criterion, an optimal actuator shape for a certain constant gain has been obtained. A refined actuator shape can be obtained if we use more elements. Table 2 lists the critical dynamic pressures λ_{cr}, maximum flutter-free dynamic pressures λ_{max}, and their ratios for different norm values of the feedback control gains determined by Fig. 5. The critical dynamic pressure in Tables 1 and 2 increases as the piezo size increases because the panel is stiffer. It is interesting to note, however, that the maximum flutter-free dynamic pressure does not necessarily increase as the patch size increases. This is true due to the nonlinearity involved in this region. Because of variation in λ_{cr} values, λ_{max} alone is not good enough to judge the control performance. The ratio $\lambda_{max}/\lambda_{cr}$, is then adopted to determine the optimal design for the piezo patch. The higher the ratio is, the better is the performance of control. For NFCG $\geq$ 80, there are four possible one-set actuator designs. The shape and location of the piezo patch and the control performance $\lambda_{max}/\lambda_{cr}$ for the four designs are shown in Fig. 6. It is clear from the Table 2 and Fig. 6 that the best design in present study is given by the patch consisting of the elements 4, 5, 7, and 8 (see Fig. 2). The dynamic pressure can be increased 4.1 times λ_{cr}. The results shown in Tables 1 and 2 reveal that the application of the NFCG not only provides the optimal actuator shape and location but also yields higher performance even for small patch of piezoelectric material (e.g., for piezo/total area $= 0.14$, $\lambda_{max}/\lambda_{cr} = 4.1$).

Figure 7 indicates the NFCG values and an actuator design for a simply supported rectangular isotropic plate ($a/b = 2$). With this design the dynamic pressure can be increased 3.9 times of $\lambda_{cr}(= 442)$.

Two-Set Actuator

The two-set piezoelectric actuator is also investigated for a simply supported square isotropic plate. The piezoelectric materials are completely covered and separated into two sets at x_s. Figure 8 shows the $\lambda_{max}/\lambda_{cr}$ varying with the normalized separation position of the two-set completely covered actuators. The $\lambda_{max}/\lambda_{cr}$ reaches its maximum at about $x_s/a = 0.5$. It is not surprising to see that the two-set
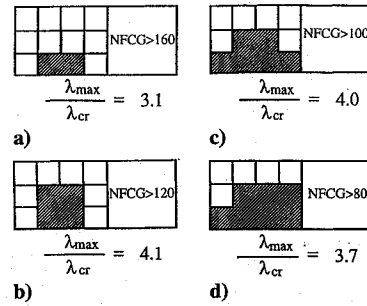

Fig. 6 One-set partially covered piezoelectric actuator designs for a simply supported square plate, $c_a = 0.01$.
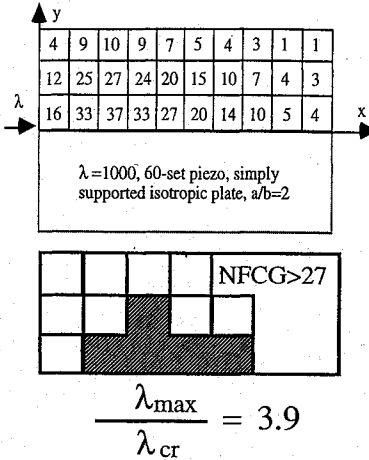

$$\frac{\lambda_{max}}{\lambda_{cr}} = 3.9$$

Fig. 7 NFCG and one-set partially covered piezoelectric actuator design for a simply supported rectangular $a/b = 2$ plate, $c_a = 0.1$.
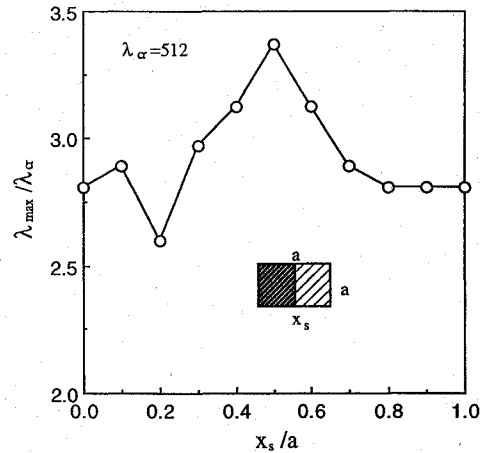

Fig. 8 Performance of two-set completely covered actuator for a simply supported square plate, $c_a = 0.01$.

piezo actuator can reach a much higher λ_{max} due to the much higher stiffness induced by the piezoelectric layers.

The effect of different boundary conditions is also studied. The NFCG and actuator designs for a clamped square isotropic plate ($a/b = 1$) are shown in Fig. 9. The maximum dynamic pressure λ_{max} is only increased for about two times the critical dynamic pressure $\lambda_{cr}(= 403)$ because the plate is much stiffer with the clamped boundary conditions. The piezos are partially covered on the top and bottom of the plate. Figure 9 shows that two-set piezoelectric actuator design is slightly better than one-set actuator design. This is true because the control effort for two-set design can be much more flexible.

Effect of Temperature

The flutter suppression is also investigated under two uniform temperature conditions which are moderate ($\Delta T/\Delta T_{cr} = 3.0$) and high ($\Delta T/\Delta T_{cr} = 6.0$) temperatures, where ΔT_{cr} denotes the
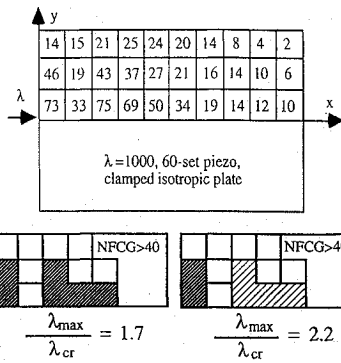
Fig. 9 NFCG and one- or two-set partially covered piezoelectric actuator design for a clamped square plate, $c_a = 0.1$.
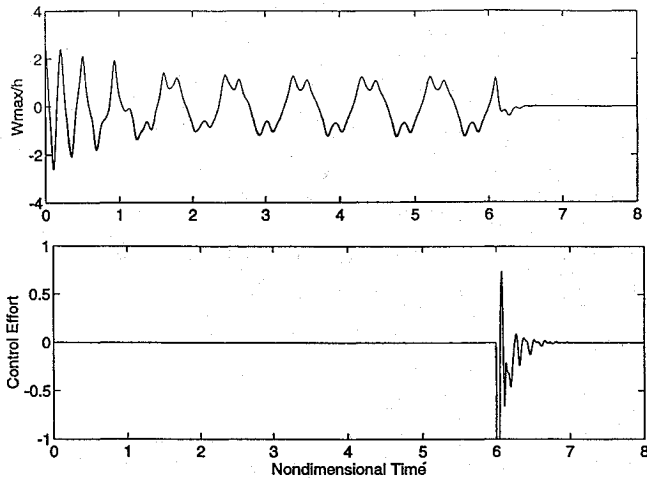

Fig. 10 Time history of periodic motion and control effort for a simply supported square panel at $\Delta T/\Delta T_{cr} = 3.0$ and $\lambda = 100, c_a = 0.1$.
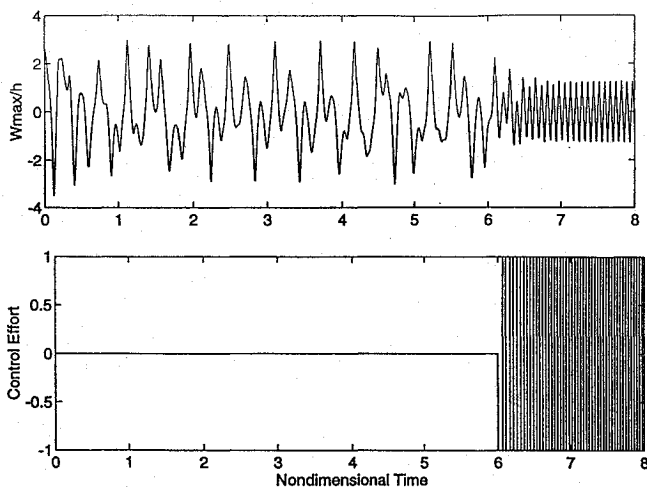

Fig. 11 Time history of chaotic motion and control effort for a simply supported square panel at $\Delta T/\Delta T_{cr} = 6.0$ and $\lambda = 200, c_a = 0.1$.

critical buckling temperature. The piezoelectric actuator configuration in Fig. 6c (NFCG > 100) is used in this study. The time history and control effort at $\Delta T/\Delta T_{cr} = 3.0$ and 6.0 are shown in Figs. 10 and 11, respectively. At the moderate temperature, the panel motion in Fig. 10 is periodic, and the flutter motion can be completely suppressed by the piezoelectric actuation. However, the panel motion is chaotic with snap-through or oil-canning behavior at high temperature as shown in Fig. 11. As the limited control effort is activated, the panel motion becomes a limit-cycle oscillation, and the peak amplitude reduces by about one-half. With increased piezoelectric actuation by using higher maximum electric field (say 80% of the depolarization) with the present configuration or thicker piezoelectric layer, the limit-cycle motion may be suppressed. Further investigations are warranted.

Conclusions

A finite element time domain–modal formulation is presented for the panel flutter suppression. The performance of flutter suppression using piezoelectric actuation is demonstrated by increasing the maximum flutter-free dynamic pressure λ_{max} or the ratio of λ_{max} to the critical dynamic pressure λ_{cr}. The linear optimal control design is based on the linear modal equations of motion whereas the numerical simulations are obtained by solving the nonlinear dynamic flutter equations. The numerical simulation shows that the in-plane force induced by piezoelectric layers is insignificant in flutter suppression. Because the operating electric field is limited (one-half of depolarization field), the use of in-plane force reduces the remaining control power for bending moment and degrades the performance. Therefore, the in-plane force is set equal to zero in all of the simulations. The optimal shape and location of the piezoelectric actuators have been determined for one particular weighting constant by considering the norms of the feedback control gain matrix as a design criterion. Once the optimal control gain is properly selected at the maximum flutter-free dynamic pressure λ_{max}, it can be used to completely suppress the flutter with any dynamic pressure lower than λ_{max}. The performance of piezoelectric isotropic plate with different boundary conditions and aspect ratios has also been studied. With optimal feedback control through a one-set partially covered piezoelectric actuator, the critical dynamic pressure can be increased about four times for simply supported isotropic plates. The critical dynamic pressure is increased only about two times for clamped squared isotropic plate because the plate is much stiffer. The two-set actuator design yields better performance than one-set actuator design because of more flexibility in control. Suppression of flutter motions, periodic and chaotic, at moderate and high temperatures is also investigated.

Appendix A: Linear and Nonlinear Stiffness Matrices

Linear stiffness terms in $\{W_b\}$ are

$$[\tilde{K}]\{W_b\} = (\lambda[A_a] + [K_b] - [K_{N\Delta T}] - [K_{Ne}])\{W_b\}$$

$$+ [K1]_{bm}[K_m]^{-1}(\{P_{m\Delta T}\} + \{P_{me}\}) \tag{A1}$$

First-order nonlinear stiffness in $\{W_b\}$ is

$$[\overline{K1}] = [K1_{Nm}]_b \tag{A2}$$

Second-order nonlinear stiffness in $\{W_b\}$ is

$$[\overline{K2}] = [K2] - [K1]_{bm}[K_m]^{-1}[K1]_{mb} \tag{A3}$$

where all the system matrices in Eqs. (A1–A3) have been defined in Eq. (21).

Appendix B: Nonlinear Modal Equations

The nonlinear stiffness matrices $[K1]_{bm}$ and $[K2]$ can be expressed in terms of the modal coordinates as

$$[K1]_{bm} = \sum_{r=1}^{n} q_r [K1]_{bm}^{(r)} \tag{B1}$$

and

$$[K2] = \sum_{r=1}^{n} \sum_{s=1}^{n} q_r q_s [K2]^{(rs)} \tag{B2}$$

where the nonlinear modal stiffness matrices $[K1]_{bm}^{(r)}$ and $[K2]^{(rs)}$ are evaluated with the normal modes $\{\phi_r\}$ and $\{\phi_s\}$. Thus, $[K1]_{bm}^{(r)}$ and $[K2]^{(rs)}$ are known matrices.

The nonlinear stiffness matrix $[K1_{Nm}]_b$ is linearly dependent on the in-plane displacement $\{W_m\}$ which can be expressed in term of the modal coordinates as

$$\{W_m\} = [K_m]^{-1}(\{P_{m\Delta T}\} + \{P_{me}\} - [K1]_{mb}\{W_b\})$$

$$= \{W_m\}_0 + \sum_{r=1}^{n} \sum_{s=1}^{n} q_r q_s \{W_m\}_{rs} \tag{B3}$$

where

$$\{W_m\}_0 = [K_m]^{-1}(\{P_{m\Delta T}\} + \{P_{me}\})$$ (B4)

$$\{W_m\}_{rs} = -[K_m]^{-1}[K1]_{mb}^{(r)}\{\phi_s\}$$ (B5)

This leads to the matrix $[K1_{Nm}]_b$ which is the sum of two matrices: the first matrix $[K_{Nm}]$ is evaluated with $\{W_m\}_0$ and the second matrix $[K2_{Nm}]^{(rs)}$ is evaluated with $\{W_m\}_{rs}$ as

$$[K1_{Nm}]_b = [K_{Nm}] + \sum_{r=1}^{n}\sum_{s=1}^{n} q_r q_s [K2_{Nm}]^{(rs)}$$ (B6)

With the modal transformation equation (25) and Eqs. (B1–B6), Eq. (22) becomes

$$M\frac{d^2q}{d\tau^2} + C\frac{dq}{d\tau} + Kq + K_eq + K_{qq}q = F$$ (B7)

where the diagonal modal mass and aerodynamic damping matrices are

$$(M, C) = \Phi^T([M_b], g_a[G])\Phi$$ (B8)

the linear terms in q are

$$Kq = \Phi^T(\lambda[A_a] + [K_b] - [K_{N\Delta T}] + [K_{Nm}])\Phi q$$

$$+ \Phi^T\left(\sum_{r=1}^{n} q_r[K1]_{bm}^{(r)}\{W_m\}_0\right)$$ (B9)

$$K_eq = -\Phi^T[K_{Ne}]\Phi q$$ (B10)

the cubic term in q is

$$K_{qq}q = \Phi^T\left\{\sum_{r=1}^{n}\sum_{s=1}^{n} q_r q_s[K2_{Nm}]^{(rs)} + \sum_{r=1}^{n}\sum_{s=1}^{n} q_r q_s[K2]^{(rs)}\right.$$

$$\left. - \sum_{r=1}^{n}\sum_{s=1}^{n} q_r q_s[K1]_{bm}^{(r)}[K_m]^{-1}[K1]_{mb}^{(s)}\right\}\Phi q$$ (B11)

and the modal force vector is

$$F = \Phi^T\{P_{be}\}$$ (B12)

Appendix C: Control Influence Matrix

The control influence matrix G in Eq. (29) can be determined as follows:

$$GU_b = \Phi^T\{P_{be}\} = \Phi^T P_c U_b$$ (C1)

where the control variable vector can be expressed as

$$U_b = \{U_{b1} \quad U_{b2} \cdots U_{bN}\}^T$$ (C2)

and the matrix related to piezoelectric actuators is given by

$$P_c = [P_1 \quad P_2 \cdots P_N]$$ (C3)

where N in the expressions represents the total number of piezoelectric actuator sets; P_i is a vector assembled from the piezoelectric element force vector, which can be written as

$$P_i = (e_{3\max})_i \sum_{\substack{\text{all} \\ \text{elements}}} (\{p_{be}\}\delta_i), \quad i = 1, 2, \ldots, N$$ (C4)

and

$$\delta_i = \begin{cases} 0, & \text{when the element does not belong to set } i \\ 1, & \text{when the element belongs to set } i \end{cases}$$ (C5)

References

[1]Bisplinghoff, R. L., and Ashley, H., *Principles of Aeroelasticity*, Wiley, New York, 1962, pp. 419, 420.

[2]Baker, R., "F-117A Structures and Dynamics Design Considerations," Plenary Session 8, AIAA Dynamics Specialist Conf., Dallas, TX, April 1992.

[3]Gray, C. E., Jr., and Mei, C., "Large Amplitude Finite Element Flutter Analysis of Composite Panels in Hypersonic Flow," *AIAA Journal*, Vol. 31, No. 6, 1993, pp. 1090–1099.

[4]Dowell, E. H., "Nonlinear Oscillations of a Fluttering Plate," *AIAA Journal*, Vol. 4, No. 7, 1966, pp. 1267–1275.

[5]Dowell, E. H., "Panel Flutter: A Review of the Aeroelastic Stability of Plates and Shells," *AIAA Journal*, Vol. 8, No. 3, 1970, pp. 385–399.

[6]Dehart, D., and Griffin, S., "Astronautical Laboratory Smart Structure/Skins Overview," *Proceedings of the First Joint U.S./Japan Conference on Adaptive Structures* (Maui, HI), Technomic, Lancaster, PA, 1990, pp. 3–10.

[7]Scott, R. C., and Weisshaar, T. A., "Controlling Panel Flutter Using Adaptive Materials," *Journal of Aircraft*, Vol. 31, No. 1, 1994, pp. 213–222.

[8]Lai, Z., Xue, D.Y., Huang, J.-K., and Mei, C., "Nonlinear Panel Flutter Suppression with Piezoelectric Actuation," *Proceedings of the Second Conference on Recent Advances in Active Control of Sound and Vibration* (Blacksburg, VA), Technomic, Lancaster, PA, 1993, pp. 863–874.

[9]Xue, D. Y., "Finite Element Frequency Domain Solution of Nonlinear Panel Flutter with Temperature Effects and Fatigue Life Analysis," *AIAA Journal*, Vol. 31, No. 1, 1993, pp. 154–162.

[10]Dixon, I. R., "Finite Element Analysis of Nonlinear Panel Flutter of Rectangular Composite Plates under a Uniform Thermal Load," M.S. Thesis, Dept. of Mechanical Engineering and Mechanics, Old Dominion Univ., Norfolk, VA, Aug. 1991.

[11]Zhou, R. C., Xue, D. Y., and Mei, C.,"A Finite Element Time Domain-Modal Formulation for Nonlinear Flutter of Composite Panels at Elevated Temperatures," *AIAA Journal*, Vol. 32, No. 10, 1994, pp. 2044–2052.

[12]Lewis, F. L., *Optimal Control*, Wiley-Interscience, New York, 1986, p. 51.